Applied Thermal Engineering 309 (2026) 133776

Contents lists available at ScienceDirect

Applied Thermal Engineering

journal homepage: www.elsevier.com/locate/apthermeng

Research Paper

A self-powered PV-TEG system for integrated hotspot monitoring and local thermal management based on thermoelectric voltage response☆

Yang Jiang [a,1], Hailiang Fei [b,1], Linfeng Zhang [a,*], Zhiyang Pei [b], Leijie Deng [b], Jingming Cai [b,c,**]

[a] School of Transportation, Southeast University, Nanjing, 211189, China
[b] School of Civil Engineering, Southeast University, Nanjing, 211189, China
[c] School of Electrical, Mechanical and Biomedical Engineering, University of Technology Sydney, Sydney, NSW, 2007, Australia

ARTICLE INFO

Keywords:
Photovoltaic–thermoelectric generator (PV–TEG)
Distributed photovoltaics
Hotspot localization
Self-powered wireless monitoring
Local thermal management

ABSTRACT

Distributed photovoltaic (PV) systems pose challenges for localized hotspot monitoring because modules are often dispersed and difficult to access. This study develops a self-powered photovoltaic–thermoelectric generator (PV–TEG) system in which a rear-side 2 × 2 TEG array integrates hotspot sensing, local thermal management, and wireless monitoring. A multiphysics model was established to characterize the coupling among hotspot position, thermoelectric voltage response, and local cooling and to construct a two-dimensional localization mapping from four-channel voltage responses. The system was then deployed on a rooftop PV array at a telecommunications facility in Taizhou, China, for outdoor validation. Numerical results showed that different hotspot positions produced spatially differentiated TEG voltage signatures, enabling coordinate reconstruction, while the local temperature reduction ranged from 8.15 to 12.40 K. Field tests from 08:00 to 18:00 showed that harvested thermoelectric energy cycled the supercapacitor between 2.8 and 4.0 V, supporting temperature and voltage acquisition and approximately 45 wireless transmissions to a mobile terminal. Infrared measurements showed that the PV–TEG structure reduced the local point temperature and regional average temperature by 7.7 and 5.4 °C, respectively, confirming its capability to mitigate local heat accumulation. For a controlled black-tape-induced hotspot-like anomaly, coordinate reconstruction yielded a two-dimensional localization error of 9.93 mm. These results demonstrate the feasibility of extending TEGs from conventional waste-heat harvesters to distributed thermal-field sensing nodes, providing a new approach to low-power online fault monitoring in distributed PV systems.

1. Introduction

Photovoltaic (PV) power generation has become a key technology for low-carbon electricity production because of its modularity, scalability, and compatibility with both centralized and distributed energy systems [1,2]. As global PV deployment continues to expand, the operational reliability of modules exposed to non-uniform outdoor conditions has attracted increasing attention [3,4]. In practical PV arrays, electrical mismatch, partial shading, surface contamination, microcracks, soldering defects, and encapsulation degradation can induce localized overheating, commonly referred to as hotspots [5–7]. Unlike a uniform temperature rise, hotspots are highly localized and may evolve rapidly with solar irradiance, wind speed, and module operating conditions. They not only reduce power output, but also accelerate encapsulant aging, intensify thermomechanical stress, and, in severe cases, create reliability and safety risks [7,8]. These challenges are particularly pronounced in distributed PV applications, including building and industrial-park rooftops, data centers, transportation infrastructure, and remote power-supply facilities, where modules are widely dispersed and some installation locations are difficult to access. Conventional manual inspection may therefore fail to identify local abnormalities in a timely manner. Timely hotspot detection and mitigation are consequently essential for ensuring the long-term stable operation of PV systems.

☆ This article is part of a Special issue entitled: 'Thermoelectric Conversion' published in Applied Thermal Engineering.

* Corresponding author at: School of Transportation, Southeast University, Nanjing, 211189, China.
** Corresponding author at: School of Electrical, Mechanical and Biomedical Engineering, University of Technology Sydney, NSW, 2007, 2007.
E-mail addresses: belzhang@seu.edu.cn (L. Zhang), Jingming.Cai@uts.edu.au (J. Cai).
[1] These authors contributed equally to this work.

https://doi.org/10.1016/j.applthermaleng.2026.133776
Received 31 July 2026; Received in revised form 4 October 2026; Accepted 21 October 2026
Available online 24 October 2026
1359-4311/© 2026 The Author(s). Published by Elsevier Ltd. This is an open access article under the CC BY license (http://creativecommons.org/licenses/by/4.0/).

Nomenclature

Abbreviation

EVA	Ethylene–vinyl acetate
HVRI	Hotspot voltage response index
PV	Photovoltaic
PV–TEG	Photovoltaic–thermoelectric generator
TEG	Thermoelectric generator
TPT	Tedlar–Polyester–Tedlar

Latin symbols

c_p	Specific heat capacity ($J \cdot kg^{-1} \cdot K^{-1}$)
e_i	Two-dimensional localization error at the i-th hotspot position (mm)
G	Solar irradiance ($W \cdot m^{-2}$)
h	Natural-convection heat-transfer coefficient ($W \cdot m^{-2} \cdot K^{-1}$)
h_i	Hotspot voltage response index of the *i*-th TEG (–)
k	Thermal conductivity ($W \cdot m^{-1} \cdot K^{-1}$)
$\mathbf{J}$	Electric current density vector ($A \cdot m^{-2}$)
N	Number of p–n thermocouple pairs (–)
P_{PV}	Electrical power generated by the PV region (W)
Q_{PV}	Baseline PV volumetric heat source ($W \cdot m^{-3}$)
Q_{hot}	Additional localized hotspot heat source ($W \cdot m^{-3}$)
Q_0	Hotspot volumetric heat-source intensity ($W \cdot m^{-3}$)
$\mathbf{q}$	Heat flux vector ($W \cdot m^{-2}$)
q''_{hot}	Equivalent hotspot heat-flux density ($W \cdot m^{-2}$)
R''_{int}	Area-normalized interfacial thermal resistance ($m^2 \cdot K \cdot W^{-1}$)
S	Seebeck coefficient ($V \cdot K^{-1}$)
S_U	Total voltage-response intensity (V)
$T_{c,i}$	Cold-side temperature of the *i*-th TEG (K)
$T_{h,i}$	Hot-side temperature of the *i*-th TEG (K)
T_{Si}	Average temperature of the silicon cell layer (K)
T_a	Ambient temperature (K)
$U_{oc,i}$	Open-circuit voltage of the *i*-th TEG (V)
(x_h, y_h)	Hotspot-center coordinates (mm)
$(\hat{x}, \hat{y})$	Reconstructed hotspot coordinates (mm)

Greek symbols

α_{Si}	Absorptance of the silicon cell layer (–)
β	PV cell temperature coefficient (K^{-1})
ΔT_{cool}	Local temperature reduction achieved by the PV–TEG configuration (K)
ΔU_i	Voltage change of the *i*-th TEG relative to its baseline value (V)
η_{PV}	Temperature-dependent PV conversion efficiency (–)
η_{ref}	PV conversion efficiency at the reference temperature (–)
ξ	Normalized horizontal voltage centroid (–)
ζ	Normalized vertical voltage centroid (–)
ρ	Material density ($kg \cdot m^{-3}$)
σ	Electrical conductivity ($S \cdot m^{-1}$)
τ_j	Transmittance of the *j*-th encapsulation layer above the silicon cell (–)
φ	Electric potential (V)

The formation of a PV hotspot fundamentally originates from the local redistribution of electrical and thermal energy. When a cell or a small region of a module operates abnormally, part of the incident solar energy and electrical mismatch loss is converted into localized heat, producing a non-uniform temperature field that differs from that of the surrounding area [9,10]. This local thermal-field distortion is generally first manifested as a high-temperature region on the front surface of the module, while corresponding perturbations in heat flux and temperature gradient also develop on the rear side. Because the rear-side thermal response is jointly governed by the module structure, contact interfaces, and heat-dissipation pathways, it contains information related to the location and thermal coupling intensity of the abnormal heat source. However, most existing PV monitoring methods primarily focus on front-surface temperature distributions or global electrical parameters and do not fully exploit the position-related information embedded in rear-side local thermal disturbances.

Existing PV hotspot-detection methods include infrared thermography, embedded temperature sensing, and electrical-feature-based diagnosis [5,11,12]. Infrared methods provide direct temperature-field visualization but generally require external equipment and suitable observation conditions [13–16], whereas dense embedded sensors increase wiring, power consumption, and system complexity [16,17]. Electrical measurements avoid additional thermal sensors but provide limited spatial information for localizing small-scale hotspots [18,19]. Meanwhile, passive cooling techniques can reduce PV temperature but do not normally provide position-dependent electrical signals for hotspot localization [20,21]. These limitations motivate a low-power approach that combines local thermal sensing, localization, and heat dissipation.

Thermoelectric generators (TEGs) convert temperature differences into electrical voltage through the Seebeck effect, allowing them to function as both energy harvesters and temperature-sensitive devices [22]. In conventional photovoltaic–thermoelectric generator (PV–TEG) systems, TEGs are installed on the rear side of PV modules to generate thermoelectric voltage from the temperature difference between the module backsheet and the cold side [23]. Previous studies have mainly focused on thermoelectric power output, reduction of PV operating temperature, heat-sink optimization, and enhancement of overall system energy yield, demonstrating strong coupling between TEGs and the rear-side heat-transfer pathway of PV modules [24–27]. In parallel, PV hotspot monitoring has mainly relied on dedicated temperature or optical sensing approaches, including distributed fiber-optic and infrared-based methods [28–30], while TEGs have also been investigated as power sources for self-powered PV monitoring nodes [31]. The spatial information contained in the distributed TEG voltage response itself, and its relation to local heat-transfer behavior, have received much less attention.

When a localized hotspot occurs, lateral heat spreading produces position-dependent thermal coupling between the hotspot and the rear-mounted TEGs, leading to spatial variations in TEG temperature difference and voltage [32,33]. The resulting multichannel voltage pattern can therefore encode the location of the thermal disturbance, while the same TEG–heat-sink pathway contributes to local heat removal [34].

Accordingly, this study develops a self-powered PV–TEG system using a rear-side 2×2 TEG array for hotspot localization, local thermal management, and intermittent wireless monitoring. Four-channel voltage responses are normalized and converted into two-dimensional hotspot coordinates, while harvested thermoelectric energy supports sensing and transmission. Numerical and outdoor experiments are used to evaluate the coupled thermal, electrical, and localization responses. The thermal-engineering contribution is to establish that local cooling and spatial thermoelectric response share the same position-dependent hotspot–TEG thermal-coupling mechanism, allowing the TEG voltage pattern to serve as an electrical indicator of local thermal coupling.

2. System design and working principle

2.1. Overall system architecture

Fig. 1 illustrates the proposed PV–TEG system, which integrates a

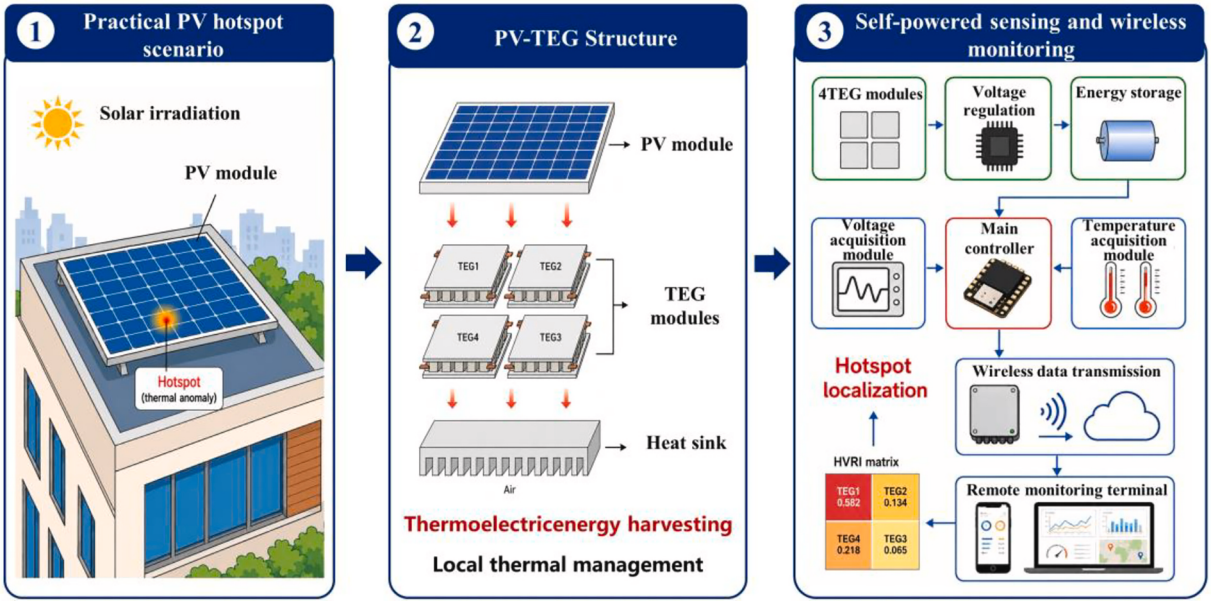


Fig. 1. Conceptual framework and operating principle of the self-powered PV–TEG system.

rear-side 2 × 2 TEG array with voltage and temperature acquisition, energy management, and wireless communication. Under uniform operating conditions, the four TEGs provide baseline voltage signals. When a localized thermal anomaly occurs, the non-uniform rear-side temperature field produces spatially differentiated temperature differences and voltage responses across the array, providing position-dependent electrical signatures for anomaly localization. Meanwhile, the harvested thermoelectric energy is stored to support intermittent sensing and wireless transmission, enabling self-powered thermal-anomaly monitoring and remote data acquisition.

2.2. *PV-TEG structural design and working principle*

The PV–TEG assembly consists of the PV module, rear-mounted TEG array, thermal interfaces, and aluminum heat sink. The TEG hot sides are coupled to the PV backsheet and the cold sides to the heat sink. This configuration simultaneously converts the PV-to-heat-sink temperature difference into electrical energy, provides position-dependent voltage responses to local thermal disturbances, and establishes an additional rear-side heat-transfer pathway for local heat dissipation.

The harvested energy is conditioned by the power-management circuit and stored in a supercapacitor. The monitoring node is activated when the capacitor reaches the upper voltage threshold and returns to charging after reaching the lower threshold, enabling duty-

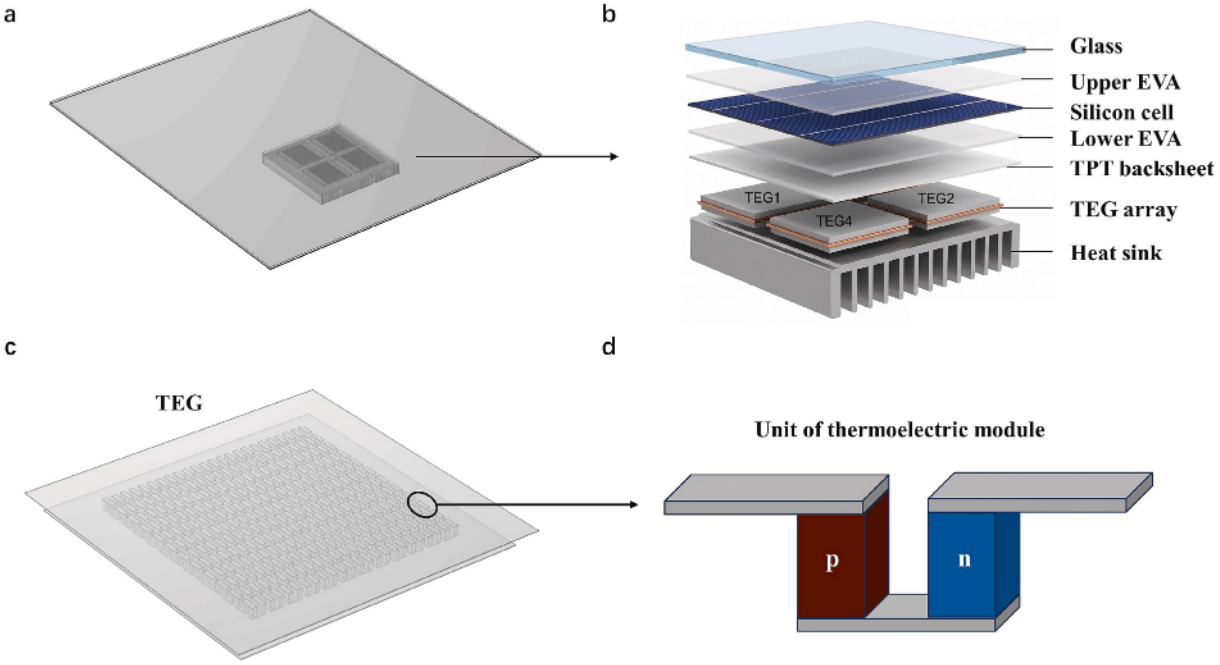


Fig. 2. Three-dimensional multiphysics model of the PV–TEG system: (a) representative PV region with the rear-side TEG array; (b) exploded layered structure; (c) detailed geometry of a TEG module; and (d) p–n thermoelectric couple.

cycled sensing and wireless transmission without continuous external power.

3. Numerical modeling and outdoor experiments

3.1. Numerical method

3.1.1. Numerical model

A three-dimensional multiphysics model of a representative local PV region, rear-side 2 × 2 TEG array, and aluminum heat sink was developed to analyze hotspot-induced heat transfer and thermoelectric response (Fig. 2). TEG1 and TEG2 form the upper row and TEG4 and TEG3 the lower row; each module contains 288 p–n thermocouple pairs.

The PV was modeled as a glass/EVA/monocrystalline-Si/EVA/TPT multilayer structure, with the TEG array coupled between the backsheet and heat sink through thermal interfaces. The model simultaneously accounts for heat conduction, thermoelectric conversion, and heat exchange with the ambient environment. Geometric and material parameters are given in Tables 1–3.

Mesh independence was assessed using coarse, normal, and fine meshes. The adopted normal mesh contained 1,663,963 tetrahedral elements, with local refinement applied to the TEG/coupling regions using a minimum prescribed element size of 0.143 mm. Refinement to 2,580,679 elements changed the PV temperature, TEG1 hot- and cold-side temperatures, and open-circuit voltage by less than 0.3%. Full convergence results are provided in Section S1.

3.1.2. Governing equations

The numerical model couples heat transfer in solids with thermoelectric effects. The temperature fields in the PV encapsulation layers, Aluminum encapsulation layer, and aluminum heat sink are governed by the energy conservation Eq. [37]:

$$\rho c_p \frac{\partial T}{\partial t} - \nabla\cdot(k\nabla T) = Q \tag{1}$$

where ρ, c_p and k denote the material density, specific heat capacity, and thermal conductivity, respectively; T is the temperature, t is time, and Q is the volumetric heat source. Because this study focuses on the quasi-steady temperature field under constant irradiance, the transient term in Eq. (1) was neglected in the steady-state simulations.

Solar radiation transmitted through the glass cover and EVA encapsulation layer is absorbed by the silicon cell layer. The fraction not converted into electricity is represented as a volumetric heat source within the silicon layer [38]:

$$Q_{PV} = \frac{GA_{PV}\alpha_{Si}\prod_j \tau_j - P_{PV}}{V_{Si}} \tag{2}$$

where G is the solar irradiance, A_{PV} is the illuminated area, α_{Si} is the absorptance of the silicon cell layer, τ_j is the transmittance of the j th encapsulation layer above the silicon layer, V_{Si} is the silicon-layer volume, and P_{PV} is the electrical power generated within the corresponding illuminated region. The PV electrical power and temperature-dependent conversion efficiency are expressed as:

$$P_{PV} = GA_{PV}\eta_{PV}(T_{Si}) \tag{3}$$

$$\eta_{PV}(T_{Si}) = \eta\left[1 - \beta\left(T_{Si} - T_{ref}\right)\right] \tag{4}$$

where η_{ref} is the PV conversion efficiency at the reference temperature T_{ref} , β is the cell temperature coefficient, and T_{Si} is the average temperature of the silicon layer.

Heat conduction, charge transport, and thermoelectric coupling occur simultaneously within the TEGs. Accounting for the Seebeck, Peltier, and Joule heating effects, the energy conservation equation is written as [39,40]:

$$\rho_{TEG} c_{p,TEG} \frac{\partial T}{\partial t} + \nabla\cdot\mathrm{q} = \mathrm{J}\cdot\mathrm{E} \tag{5}$$

where **q** is the heat-flux density, **J** is the current density, $\mathbf{E} = -\nabla\varphi$ is the electric field, and φ is the electric potential. The heat-flux and current densities are governed by:

$$\mathrm{q} = -k_{TEG}\nabla T + ST\mathrm{J} \tag{6}$$

$$\nabla\cdot\mathrm{J} = 0 \tag{7}$$

$$\mathrm{J} = \sigma(-\nabla\varphi + S\nabla T) \tag{8}$$

where S and σ denote the Seebeck coefficient and electrical conductivity, respectively. The temperature-dependent expressions for k_{TEG} , S, and σ of the p- and n-type thermoelectric materials are given in Table 3.

Each TEG module comprises $N = 288$ p–n thermocouple pairs. Under open-circuit conditions, the output voltage of the ith TEG is determined by the temperature difference between its hot and cold sides and the Seebeck coefficients of the p- and n-type thermoelectric materials [41]:

$$U_{oc,i} = N\int_{T_{c,i}}^{T_{h,i}} \left[S_p(T) - S_n(T)\right]dT \tag{9}$$

where $T_{h,i}$ and $T_{c,i}$ are the hot- and cold-side temperatures of the ith TEG, respectively, and $S_p(T)$ and $S_n(T)$ are the temperature-dependent Seebeck coefficients of the p- and n-type thermoelectric materials.

The contact thermal resistances at the PV backsheet–TEG hot-side and TEG cold-side–aluminum heat-sink interfaces were represented using equivalent thin layers. The normal heat-flux density across an interface is given by:

$$q_n = \frac{T_1 - T_2}{R''_{\mathrm{int}}} \tag{10}$$

For an equivalent interfacial layer with thickness t_{int}, the corresponding effective thermal conductivity is expressed as [42]:

$$k_{\mathrm{int}} = \frac{t_{\mathrm{int}}}{R''_{\mathrm{int}}} \tag{11}$$

where R''_{int} denotes the area-specific interfacial thermal resistance.

3.1.3. Assumptions and boundary conditions

All solid components were treated as homogeneous and isotropic. Material properties were assumed constant except for the temperature-dependent thermal conductivity, electrical conductivity, and Seebeck coefficient of the thermoelectric materials. Mass transport was neglected, and the PV–TEG and TEG–heat-sink contact resistances were represented by equivalent thin layers [43].

Both the ambient and initial temperatures were set to 25 °C, and the solar irradiance incident on the PV front surface was fixed at 1000 W·m^{-2} [44]. The fraction of absorbed solar energy not converted into electricity was applied to the silicon cell layer according to Eq. (2).

Table 1
Geometric specifications of the PV–TEG numerical model [35].

Structure	Component	Design dimensions (mm)
PV	Glass Cover	500 × 500 × 3
	Top EVA encapsulant	500 × 500 × 0.4
	Silicon solar cell	500 × 500 × 0.18
	Bottom EVA encapsulant	500 × 500 × 0.4
	TPT backsheet	500 × 500 × 0.18
	Aluminum encapsulation layer	40 × 45 × 0.1
TEG	p-type elements	0.8 × 0.8 × 1.5
	n-type elements	0.8 × 0.8 × 1.5
	Copper layer	0.8 × 1.6 × 0.1
Sink	Heat sink base	150 × 150 × 4
	Heat sink fins	1.5 × 150 × 12

Table 2
Thermophysical and optical properties of the PV–TEG model components [36].

Structure	Component	Density (kg/m^3)	Specific heat capacity (J/kg·K)	Thermal conductivity (W/m·K)	Absorptance α	Transmittance τ
PV	Glass Cover	2450	500	2	0.04	0.92
	EVA encapsulant	960	2090	0.311	0.02	0.98
	Silicon solar cell	2330	712	130	0.9	/
	TPT backsheet	1200	1250	0.15	0.01	/
Sink	Aluminum	2700	900	238	/	/

Table 3
Thermoelectric properties of TEG [36].

Component	Thermal conductivity (W/m·K)	Electrical conductivity (S·m^{-1})	Seebeck coefficient (V/K)
Aluminum encapsulation layer	238	3.774×10^7	/
p-type elements	3.62×10^{-5} T^2–0.0264 T + 6.22	$(0.0156T^2–15.71\ T + 4466.38) \times 10^2$	$(-3.64 \times 10^{-3}\ T^2 + 2.74\ T - 296.21) \times 10^{-6}$
n-type elements	3.35×10^{-5} T^2–0.0234 T + 5.61	$(0.0106T^2–10.16\ T + 3113.71) \times 10^2$	$(1.53 \times 10^{-3}\ T^2–1.08\ T - 28.34) \times 10^{-6}$
Copper layer	400	5.998×10^7	/

Natural-convection boundary conditions were imposed on the irradiated PV surface and the heat-sink surfaces exposed to the ambient environment [45]:

$$-\mathrm{n}\cdot\mathrm{q} = h(T - T_a) \tag{12}$$

where **n** is the outward unit normal vector, q is the heat-flux vector, h is the natural-convection heat-transfer coefficient, and T_a is the ambient temperature. Under the Typical condition, h = 10 W·m^{-2}·K^{-1} was adopted as the effective natural-convection coefficient for the exposed PV and heat-sink surfaces, consistent with values commonly used for natural-convection and light-wind ambient conditions [46,47]. Because the effective convective heat transfer may vary with ambient airflow and surface conditions, additional values of h = 5 and 15 were considered together with the Typical-condition value in the sensitivity analysis presented in Section 4.1.4. All remaining external boundaries without direct heat exchange with the environment were treated as adiabatic:

$$-\mathrm{n}\cdot\mathrm{q} = 0 \tag{13}$$

The bare PV and PV–TEG configurations were subjected to identical solar irradiance, ambient temperature, natural-convection, and hotspot conditions. For the nine hotspot cases P1–P9, only the hotspot-center coordinates were varied, while the hotspot dimensions, heat-source intensity, material properties, interfacial thermal resistances, and mesh settings were kept unchanged to ensure comparability among different hotspot locations.

3.1.4. Hotspot modeling and thermoelectric-voltage localization

To investigate the effects of localized thermal anomalies on the PV temperature field and the distributed TEG voltage response, an additional localized heat source was superimposed within the silicon cell layer. The total volumetric heat source in the silicon layer is expressed as:

$$Q_{total} = Q_{PV} + Q_{hot}(x, y) \tag{14}$$

where Q_{PV} is the baseline heat source under uniform irradiance and Q_{hot} is the additional localized hotspot heat source. The hotspot-affected region was defined using a smooth spatial window:

$$Q_{hot}(x, y) = Q_0 f_x(x; x_h, w_h, s_h) f_y(y; y_h, w_h, s_h) \tag{15}$$

where Q_0 is the hotspot heat-source intensity, (x_h, y_h) denotes the hotspot-center coordinates, w_h is the characteristic hotspot dimension, and s_h is the boundary-smoothing parameter. The hotspot dimensions and heat-source intensity were kept constant for all scanning cases [48]. The localized hotspot was defined as a 20 mm × 20 mm rectangular region in the silicon cell layer, corresponding to an area of 400 mm^2. An equivalent hotspot heat-flux density of q''_{hot}=5000 W/m^2 was adopted, corresponding to a nominal additional thermal power of 2.0 W over the hotspot area. Because the heat source was applied within the 0.18-mm-thick silicon layer, the corresponding volumetric heat-source intensity was $Q_0 = 2.78 \times 10^7$ W·m^{-3}. The hotspot size and thermal loading were kept unchanged for all P1–P9 cases, with only the hotspot-center coordinates varied.

Nine hotspot locations were defined in a 3 × 3 grid within the 500 mm × 500 mm local PV region, with P5 taken as the coordinate origin. Their coordinates were:

$$\begin{aligned} &\mathrm{P1} = (-100, 75)\ \mathrm{mm}, \mathrm{P2} = (0, 75)\ \mathrm{mm}, \mathrm{P3} = (100, 75)\ \mathrm{mm} \\ &\mathrm{P4} = (-100, 0)\ \mathrm{mm}, \mathrm{P5} = (0, 0)\ \mathrm{mm}, \mathrm{P6} = (100, 0)\ \mathrm{mm} \\ &\mathrm{P7} = (-100, -75)\ \mathrm{mm}, \mathrm{P8} = (0, -75)\ \mathrm{mm}, \mathrm{P9} = (100, -75)\ \mathrm{mm} \end{aligned} \tag{16}$$

The scanning scheme covered four corner positions, four edge-center positions, and one central position. The spatial arrangement of the TEG array was fixed as:

$$\begin{pmatrix} TEG1 & TEG2 \\ TEG4 & TEG3 \end{pmatrix} \tag{17}$$

The local thermal-management performance was evaluated using the average temperature of the silicon cell layer:

$$T_{Si} = \frac{1}{V_{Si}} \int_{V_{Si}} T dV \tag{18}$$

The local temperature reduction achieved by the PV–TEG configuration relative to the bare PV configuration was defined as:

$$\Delta T_{cool} = T_{Si,barePV-} T_{Si,PV-TEG} \tag{19}$$

Hotspot localization was referenced to the open-circuit voltages of the TEGs under the hotspot-free condition. The voltage change of the i th TEG under a hotspot condition was defined as:

$$\Delta U_i = U_{i,hot} - U_{i,baseline} \tag{20}$$

Using voltage changes relative to the baseline reduces the influence of differences in the initial TEG voltages, local contact conditions, and boundary conditions on spatial inference [28,29]. The total voltage-response intensity induced by the hotspot was defined as:

$$S_U = \sum_{i=1}^{4} |\Delta U_i| \tag{21}$$

The voltage change of each channel was then normalized to obtain

the hotspot voltage response index (HVRI):

$$h_i = HVRI_i = \frac{|\Delta U_i|}{S_U} \tag{22}$$

According to the actual spatial arrangement of the TEGs, the HVRI matrix was expressed as:

$$\mathrm{H} = \begin{pmatrix} h_1 & h_2 \\ h_4 & h_3 \end{pmatrix} \tag{23}$$

S_U characterizes the overall intensity of the hotspot-induced voltage disturbance, whereas the HVRI values quantify the relative contributions of the four TEGs to the total response. The maximum HVRI identifies the dominant response channel but is insufficient to determine continuous two-dimensional hotspot coordinates.

To extract directional information from the four-channel voltage responses, normalized voltage centroids were defined in the horizontal and vertical directions, respectively:

$$\xi = (h_1 + h_3) - (h_1 + h_4) \tag{24}$$

$$\zeta = (h_1 + h_2) - (h_3 + h_4) \tag{25}$$

here, $\xi < 0$ and $\xi > 0$ indicate that the hotspot is located toward the left and right sides of the array, respectively, whereas $\zeta > 0$ and $\zeta < 0$ indicate that it is located toward the upper and lower sides, respectively. Based on the simulated results for P1–P9, linear mappings between the voltage centroids and the actual coordinates were established using the least-squares method:

$$\hat{x} = a_x \xi + b_x \tag{26}$$

$$\hat{y} = a_y \zeta + b_y \tag{27}$$

where a_x, b_x, a_y and b_y are regression coefficients obtained from the nine simulated positions, and $\hat{x}$ and $\hat{y}$ are the reconstructed hotspot coordinates. Because all nine positions were used both to establish the coordinate mapping and to reconstruct their coordinates, the reported localization errors represent the overall fitting-based reconstruction errors.

The two-dimensional localization error for the i th hotspot position was defined as:

$$e_i = \sqrt{(\hat{x}_i - x_i)^2 + (\hat{y}_i - y_i)^2} \tag{28}$$

3.2. Outdoor experimental validation

Outdoor experiments were conducted to evaluate self-powered wireless monitoring, local thermal management, and voltage-based localization of hotspot-like thermal disturbances using the prototype described in Section 2.

3.2.1. Daytime self-powered wireless monitoring test

The self-powered monitoring test was conducted from approximately 08:00 to 18:00. TEG hot and cold side temperatures, supercapacitor voltage, and sensing/wireless activation events were recorded throughout the test. The node was activated at approximately 4.0 V and returned to charging at approximately 2.8 V. Three parallel PV–TEG systems were independently tested ($n = 3$); because their charge–discharge events were asynchronous, Fig. 7 presents the trial whose overall operating characteristics were closest to the median response of the three experiments.

3.2.2. Outdoor infrared thermography and hotspot-like anomaly tests

Outdoor infrared thermography was used to evaluate the local thermal-management effect of the PV–TEG configuration. The temperature distribution of the PV–TEG region was compared with that of a reference PV region without rear-side TEG integration under similar orientation and tilt conditions. Local point temperatures and average temperatures over a 500 mm × 500 mm region of interest (ROI) centered on the TEG installation area were extracted from the infrared images. The comparison was independently repeated in three paired PV–TEG/reference-PV experiments ($n = 3$), with trial-level statistics provided in Section S5 of the Supplementary Information.

Voltage-based localization was evaluated using controlled black-tape-induced hotspot-like thermal anomalies. The tape was attached to the PV front surface to enhance local solar absorption and generate a repeatable thermal disturbance rather than to reproduce the electro-thermal mechanism of an actual PV hotspot. Anomalies were tested at P1 (−100, 75), P3 (100, 75), and P7 (−100, −75) mm using the same local coordinate system as the numerical model, with three independent trials conducted at each position. Infrared thermography was used to verify the anomaly location and temperature, and each trial included baseline acquisition, tape application and stabilization, infrared and four-channel TEG measurements, followed by tape removal and recovery to the no-anomaly state.

For each trial, the four TEG voltage changes were referenced to the corresponding no-anomaly baseline and normalized using the hotspot voltage response index (HVRI). The horizontal and vertical voltage centroids, ξ and ζ, were calculated according to Eqs. (24) and (25), and the anomaly coordinates were reconstructed using Eqs. (26) and (27). Localization error was defined as the Euclidean distance between the reconstructed and prescribed coordinates. Position-level mean and sample SD values were calculated from the three repeated trials, while the overall localization error was evaluated using all nine trials; detailed results are provided in Section S5.

4. Results and discussion

4.1. Numerical results

4.1.1. Baseline thermal management and thermoelectric response

To quantify the thermal-management effect of the PV–TEG configuration under hotspot-free baseline conditions, the conventional PV and PV–TEG configurations were first compared numerically. Figs. 3(a) and 3(b) present their temperature distributions, while Fig. 3(c) shows the open-circuit voltage distribution of the four TEG modules. The corresponding average temperatures and TEG open-circuit voltages are summarized in Fig. 3(d). Compared with the conventional PV configuration, the PV–TEG configuration reduced the average temperature from 346.14 to 334.07 K, corresponding to a decrease of 12.07 K. This result indicates that the TEG array and heat sink effectively modify the local heat-transfer pathway at the rear of the PV module [31].

The temperature reduction arises primarily from the additional heat-conduction pathway introduced by the PV–TEG assembly. In the conventional PV configuration, part of the absorbed solar energy is converted into heat within the PV layers. Without an effective heat-dissipation pathway, this heat accumulates in the silicon cell and backsheet, increasing the module temperature. After integrating the TEGs, thermal interfaces, and heat sink, heat is conducted from the PV rear surface through the TEG hot and cold sides and subsequently dissipated to the ambient environment through the heat sink. This pathway suppresses local heat accumulation and provides more effective passive cooling within the PV–TEG region. The PV–TEG configuration can therefore generate a thermoelectric voltage while also offering the potential to mitigate localized overheating and temperature-related performance degradation [23].

The hotspot-free open-circuit voltages of TEG1–TEG4 were approximately 1.47, 1.47, 1.46, and 1.46 V, respectively (Fig. 3(d)), indicating a nearly uniform baseline response. These values were subsequently used to calculate hotspot-induced voltage changes, HVRI values, and normalized voltage centroids.

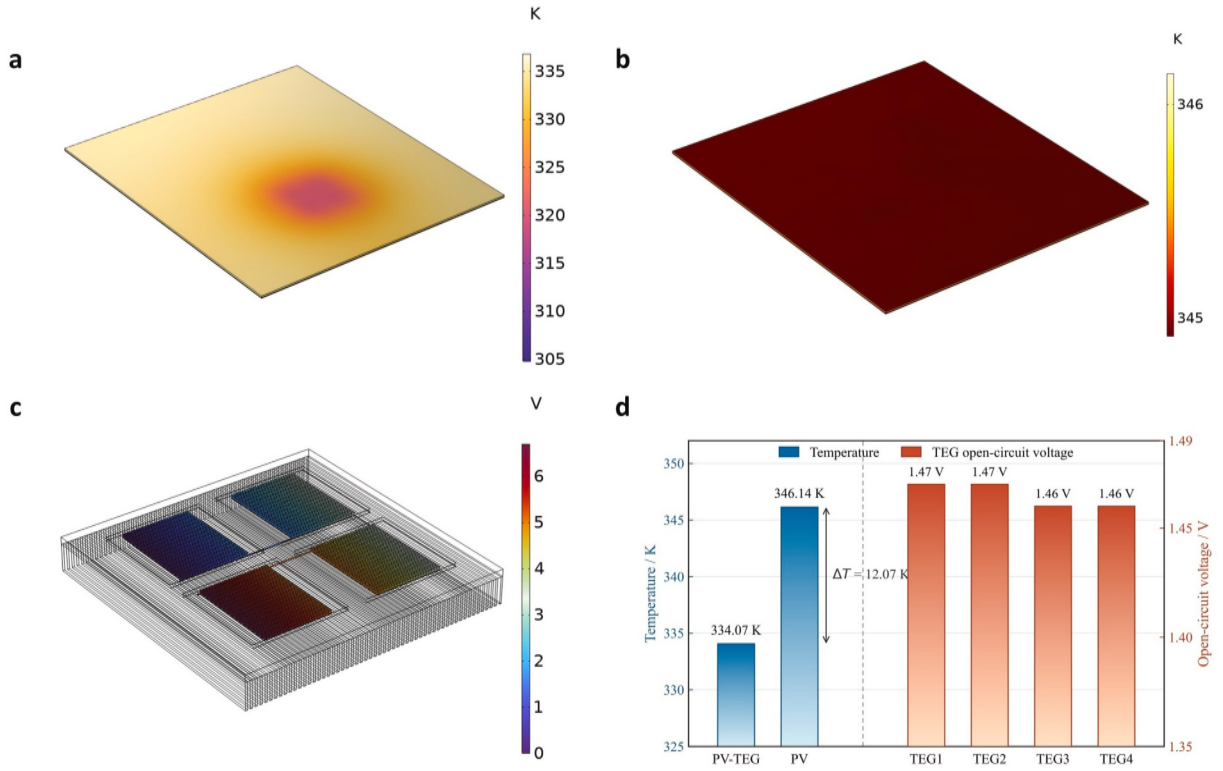


Fig. 3. Baseline thermal and thermoelectric responses under uniform irradiation: (a) temperature field of the PV–TEG configuration; (b) temperature field of the bare PV configuration; (c) open-circuit voltage of the 2 × 2 TEG array; and (d) comparison of the average PV temperatures and TEG open-circuit voltages.

4.1.2. Two-dimensional hotspot localization using normalized voltage centroids

Fig. 4(a) shows the P1–P9 calibration positions and the 2 × 2 TEG-array layout defined in Section 3.1.4. The 3 × 3 scanning pattern was used to examine the spatial variation of the four-channel thermoelectric response in both horizontal and vertical directions. Fig. 4(b) shows distinct four-channel HVRI fingerprints for different hotspot positions. At the four corner positions, the TEG nearest the hotspot produced the dominant response, whereas intermediate positions produced more balanced responses between adjacent channels; the central position P5 approached an approximately uniform four-channel distribution. This systematic shift in the dominant response demonstrates the spatial sensitivity of the TEG array. As shown in Fig. 4(c), the signs of ξ and ζ consistently distinguish the left/right and upper/lower hotspot directions, respectively. The nine calibration positions retain the topology of the physical 3 × 3 scanning grid in the $\xi - \zeta$ feature space, with P5 located near the origin, demonstrating that the normalized voltage centroids encode the two-dimensional hotspot direction.

The P1–P9 results were then used to establish the linear voltage-centroid-to-coordinate mappings described in Eqs. (26) and (27). Applying the fitted mappings back to the nine calibration positions resulted in a mean reconstruction error of 6.24 mm, a maximum error of 10.56 mm, and an RMSE of 6.60 mm. These results evaluate the accuracy of the fitted mapping on the calibration positions. The corresponding fitting-based reconstruction results are provided separately in Fig. S1 of the Supplementary Information.

To independently evaluate the established mapping at locations not used for calibration, three additional hotspot positions, V1 (−50, 37.5) mm, V2 (50, 37.5) mm and V3 (0, −37.5) mm, were introduced. These positions were excluded from the P1–P9 calibration dataset. The hotspot size and heat-source intensity, material properties, interfacial parameters, TEG geometry, and mesh settings were kept unchanged, and the mapping coefficients established from P1–P9 were applied directly to V1–V3 without refitting.

As shown in Fig. 4(d), the reconstructed coordinates of V1–V3 were (−55.30, 41.20), (55.80, 33.10), and (−4.20, −41.60) mm, respectively, corresponding to localization errors of 6.46, 7.28, and 5.87 mm. The resulting mean validation error was 6.54 mm, with an RMSE of 6.56 mm and a maximum error of 7.28 mm. All three validation positions retained the correct spatial direction. The corresponding four-channel HVRI distributions and detailed voltage-centroid calculations are provided in Fig. S2 and Tables S2–S4 of the Supplementary Information. These results demonstrate that the mapping established from P1–P9 can also reconstruct hotspot positions that were not involved in its calibration within the present numerical sensing region.

4.1.3. Location-dependent TEG voltage response and local cooling

Because hotspot position governs both thermoelectric response and heat transfer through the rear-side TEG–heat-sink pathway, Fig. 5 compares the location dependence of voltage-response intensity and local cooling. Figs. 5(a) and 5(b) compare the temperature fields of the PV–TEG and bare PV configurations under the P7 hotspot condition. In the PV–TEG configuration, the prescribed 20 mm × 20 mm hotspot produced a peak silicon temperature of 346.10 K, while the average silicon-layer temperature decreased from 346.50 K for the bare PV to 337.20 K, corresponding to a reduction of 9.30 K. This confirms the local thermal-management effect of the TEG array and heat sink. Experimentally reported PV hotspot temperatures vary with module configuration, shading ratio, and operating conditions. Zhang et al. [49] reported a maximum hotspot temperature of 348.65 K for a half-cell PV module under partial shading, while Liu et al. [50] observed a hotspot temperature of 350.81 K under 50% local shading. Similar outdoor experiments have also reported hotspot temperatures around 343.15 K under mild partial-shading conditions [51]. The simulated peak temperature of 346.10 K in the present study agrees well with the hotspot temperatures experimentally reported under comparable partial-shading conditions, supporting the physical reasonableness of the adopted hotspot intensity.

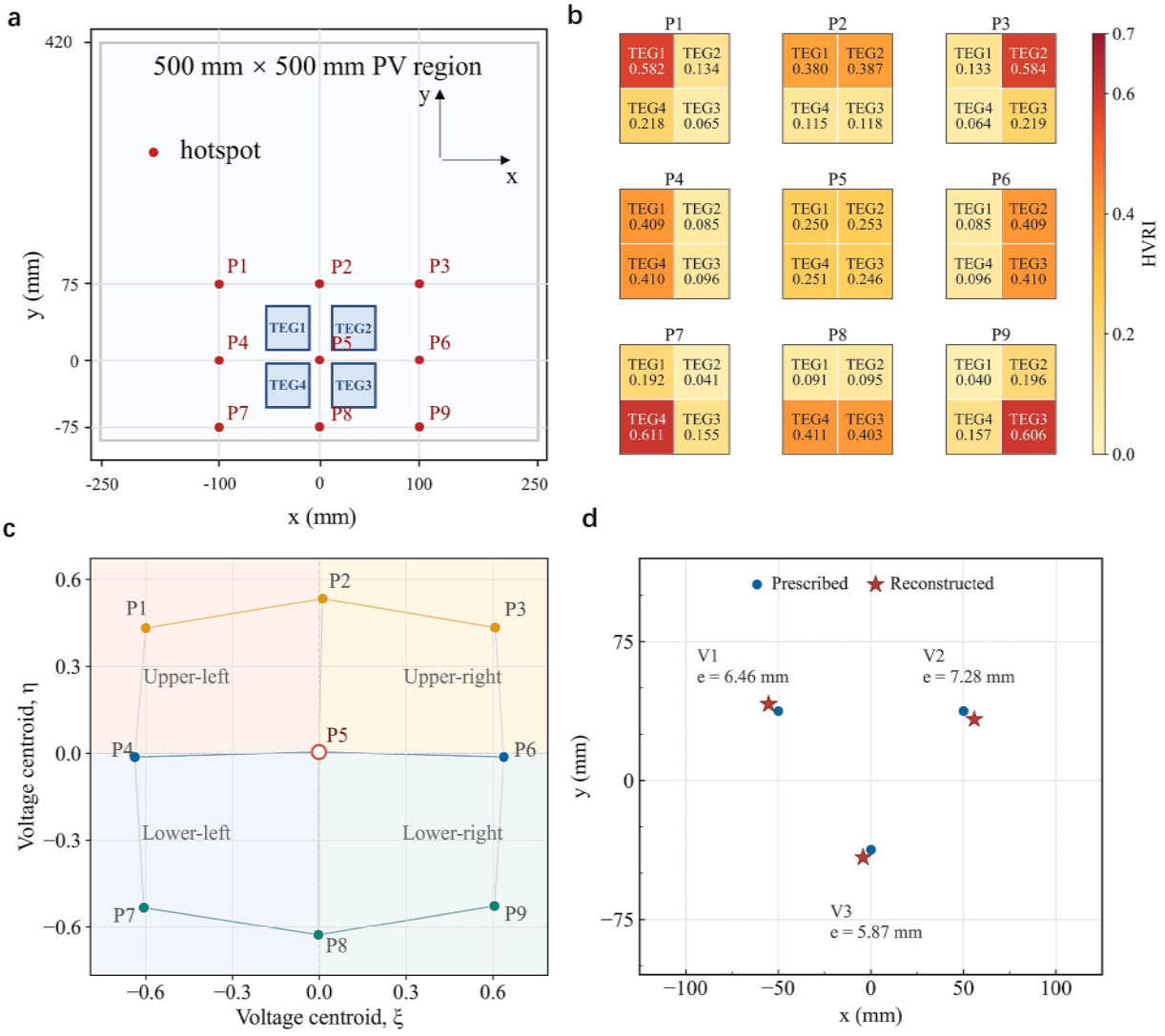


Fig. 4. Two-dimensional hotspot localization and independent numerical validation based on normalized thermoelectric voltage centroids: (a) P1–P9 calibration positions and TEG-array layout; (b) HVRI matrices for the P1–P9 calibration positions; (c) distribution of P1–P9 in the ξ – ζ feature space; and (d) comparison between the prescribed and reconstructed coordinates of the independent validation positions V1–V3.

As shown in Fig. 5(c), the local temperature reduction varied from 8.15 to 12.40 K across P1–P9, with an average of 9.93 K and the maximum reduction at the central position P5. The stronger cooling near the effective TEG heat-transfer region confirms the position dependence of local thermal management.

Fig. 5(d) shows a positive relationship between the total voltage-response intensity and local cooling magnitude. Linear regression yielded $R^2 = 0.719$ and $r = 0.848$, indicating that hotspot positions associated with stronger voltage responses generally also exhibited greater local cooling. Importantly, this relationship does not imply that the voltage response causes cooling; rather, both responses originate from the same position-dependent hotspot–TEG thermal coupling. A hotspot more effectively coupled to the rear-side TEG–heat-sink pathway simultaneously produces stronger local heat extraction and a larger thermoelectric response. This reveals a common thermal origin of the sensing and cooling functions and shows that the distributed TEG voltage can serve as an electrical descriptor of local heat-transfer coupling, rather than merely as an energy-harvesting output. The present 2 × 2 TEG array is intended as a local sensing and thermal-management node rather than a full-module coverage solution. For full-size PV modules, multiple nodes would need to be distributed over regions susceptible to localized overheating, with each node providing local voltage-response and thermal information. Scaling to such a distributed architecture would require further optimization of node spacing, sensing-area overlap, inter-node thermal interaction, calibration of the voltage–position mapping, and coordinated energy management.

4.1.4. Sensitivity of thermal and thermoelectric responses to boundary and interfacial conditions

The preceding analyses were conducted under the Typical-condition boundary settings and fixed interfacial parameters. To evaluate the effects of variations in environmental boundary conditions and interfacial heat-transfer conditions on the system response, twelve representative cases were defined at the fixed hotspot position P1(−100, 75) mm (Table 4). C0 is defined as the Typical condition; G1–G2, T1–T2, H1–H2, and R1–R2 vary the solar irradiance G, ambient temperature T_a, convective heat-transfer coefficient h, and interfacial thermal resistance R''_{int}, respectively, while M1–M3 represent typical morning, midday, and evening meteorological combinations during the outdoor test period. The complete thermal, thermoelectric, voltage-response, and localization results for all cases are provided in Tables S5–S7 of the Supplementary Information.

Changes in the boundary conditions first affect the absolute

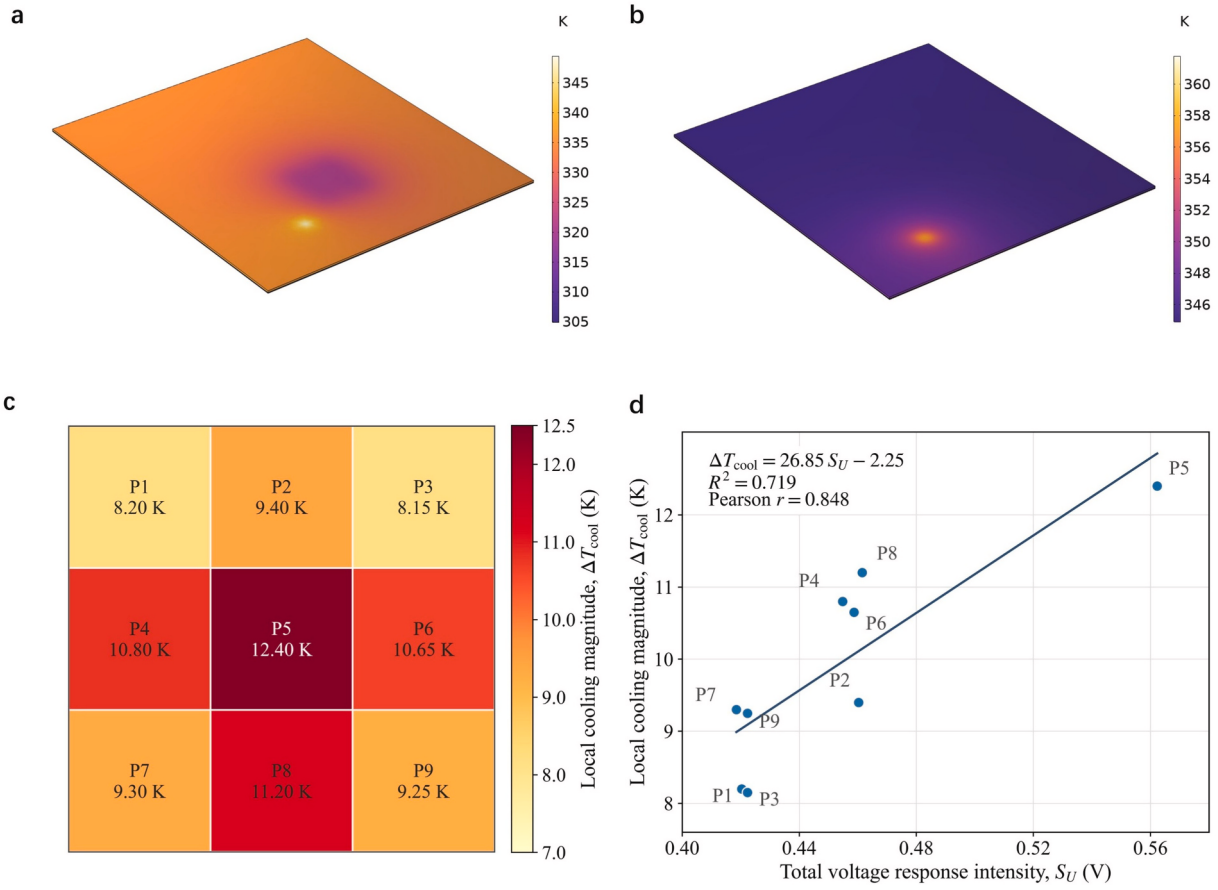


Fig. 5. Spatial dependence of the TEG voltage response and local thermal management on hotspot position: (a) temperature field of the PV–TEG configuration at P7; (b) temperature field of the bare PV configuration at P7; (c) local cooling magnitude for P1–P9; and (d) relationship between the total voltage response intensity and local cooling magnitude.

Table 4
Definitions of the twelve cases.

Case	Type	G (W m^{-2})	T_a (°C)	h (W m^{-2} K^{-1})	R''_{int}(m^2 K W^{-1})	Description
C0	Typical condition	1000	25.0	10	1.0e-04	Reference condition for comparison
G1	Irradiance	200	25.0	10	1.0e-04	Low irradiance
G2	Irradiance	600	25.0	10	1.0e-04	Intermediate irradiance
T1	Ambient T	1000	28.0	10	1.0e-04	Higher ambient temperature
T2	Ambient T	1000	31.0	10	1.0e-04	Highest ambient temperature
H1	Convection	1000	25.0	5	1.0e-04	Weaker convection
H2	Convection	1000	25.0	15	1.0e-04	Stronger convection
R1	Interface	1000	25.0	10	1.0e-05	Lower interface resistance
R2	Interface	1000	25.0	10	5.0e-04	Higher interface resistance
M1	Real-weather	445	24.3	10	1.0e-04	Representative morning combination
M2	Real-weather	992	29.5	10	1.0e-04	Representative midday combination
M3	Real-weather	206	26.2	10	1.0e-04	Representative evening combination

temperature level and thermoelectric output of the system. As the irradiance increases, the average silicon-layer temperature, hotspot peak temperature, TEG1 temperature difference, and open-circuit voltage all increase. An increase in ambient temperature mainly shifts the overall system temperature to a higher level, whereas convection and interfacial thermal resistance influence the PV temperature, TEG temperature difference, and local cooling performance by modifying the heat-transfer pathway. Despite the variations in absolute response magnitude, Fig. 6 (a) shows that TEG1 remains the dominant response channel under all cases, with HVRI values ranging from 0.568 to 0.619. The corresponding horizontal voltage centroid ξ remains negative and the vertical voltage centroid ζ remains positive, indicating that the hotspot fixed at P1 consistently retains its upper-left directional signature.

To further evaluate the effect of boundary-condition variations on coordinate reconstruction, the same voltage-centroid-to-spatial-coordinate mapping established from P1–P9 under the Typical condition (C0) was applied to all cases without recalibration. Figs. 6(b) and 6 (c) show the localization errors and reconstructed-coordinate deviations, respectively. Under C0, the reconstructed coordinate of P1 is (−97.59, 67.28) mm, corresponding to a localization error of 8.08 mm, while the errors across all cases range from 1.90 to 13.52 mm. These results indicate that variations in boundary and interfacial parameters can affect the absolute thermal response, thermoelectric output, and reconstructed coordinates, whereas the directional characteristics derived from the relative four-channel voltage distribution remain stable within the investigated range, suggesting a certain degree of

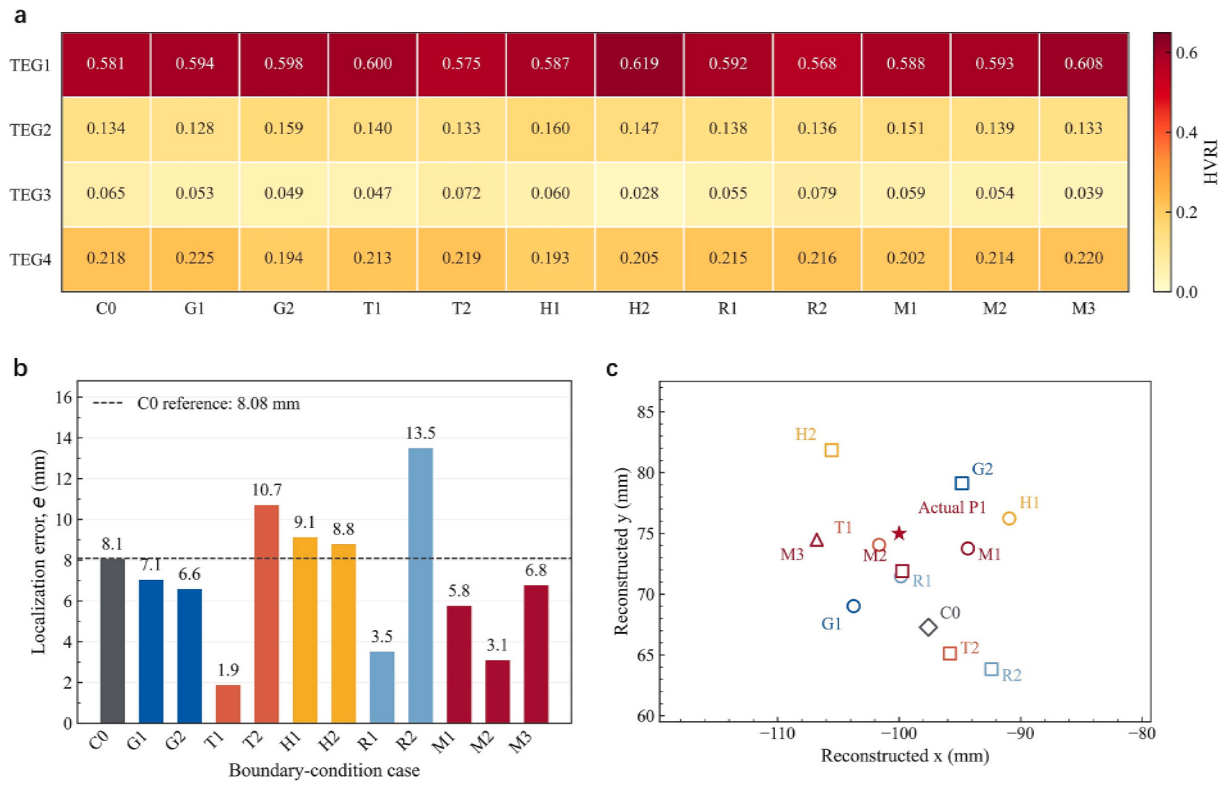


Fig. 6. Boundary-condition sensitivity of voltage-based localization at P1: (a) four-channel HVRI distributions; (b) localization errors, with the C0 value shown as a dashed reference; and (c) reconstructed positions around the prescribed P1 position.

adaptability of the proposed localization method to variations in environmental boundary conditions.

4.2. Outdoor experimental validation

4.2.1. Self-powered wireless monitoring

Fig. 7 presents the outdoor daytime validation of the self-powered PV–TEG wireless monitoring system. Fig. 7(a) shows the fully deployed prototype, including the PV module, rear-mounted PV–TEG assembly, power-management unit, supercapacitor, data-acquisition circuit, and wireless communication module. The outdoor results demonstrate that the node can harvest energy in situ from the temperature difference between the PV backsheet and the heat-dissipation side, thereby supporting intermittent data acquisition and wireless transmission. Fig. 7(b) shows the mobile receiving interface, which displays the transmitted measurements and communication status. These results confirm the complete operational chain from thermoelectric energy harvesting and power management to multiparameter acquisition and wireless data reception. The PV–TEG node therefore provides a low-power, self-powered platform for outdoor PV condition monitoring without additional external power cabling.

As shown in Figs. 7(c) and 7(d), the TEG temperatures and the corresponding meteorological conditions exhibited clear daytime variations. Both temperatures increased gradually during the morning, developed a relatively large temperature difference around midday and early afternoon, and subsequently decreased as irradiance weakened. This temperature difference directly governed the TEG energy output and the charging rate of the supercapacitor. Fig. 7(e) further shows the supercapacitor voltage from 08:00 to 18:00. When the voltage increased to approximately 4.0 V, the system was activated to acquire and transmit data. Once the voltage decreased to approximately 2.8 V, transmission ceased and the node returned to the charging state. The resulting periodic slow-charging and rapid-discharging behavior verifies the self-powered operating cycle of waste-heat harvesting, energy storage, intermittent sensing, and wireless transmission. During the daytime test, the system completed approximately 45 wireless transmission cycles. The larger TEG temperature difference around midday increased the supercapacitor charging rate and shortened the triggering interval, whereas the smaller temperature differences in the morning and evening progressively extended the interval between transmissions.

To evaluate the self-powered operation of the system, the 0.47 F, 5.0 V supercapacitor was used as the energy-storage unit, with 4.0 and 2.8 V defined as the activation and shutdown thresholds, respectively, corresponding to a nominal capacitor-energy window of 1.9176 J. For the selected complete operating cycle, an 8-min recharge period and a 150 s active period were used for the energy analysis. During recharge, approximately 2.680 J of electrical energy from the TEG array was required to deliver 1.943 J at the harvester output, of which 1.9176 J was stored in the supercapacitor and 0.0253 J was consumed by the standby load. During the subsequent active period, the identified sensing, control, and wireless-communication demand was approximately 1.2740 J, accounting for 66.4% of the nominal capacitor-energy window, with MCU processing/control representing the largest contribution. The remaining 0.6436 J represents an unresolved energy balance associated with unquantified peripheral-circuit consumption and conversion/storage effects. The detailed operating parameters, calculation procedure, and component-level energy accounting are provided in Section S4 and Tables S8–S9, while Fig. S4 summarizes the active-stage energy distribution and the relationship between net capacitor-charging power and the TEG temperature difference.

4.2.2. Infrared validation of local thermal management and hotspot localization

Fig. 8(a–c) compares the local thermal responses of the PV–TEG and reference PV regions. Representative infrared thermograms are shown in Fig. 8(b), while Fig. 8(c) summarizes the results of three independent paired experiments. The mean local point temperatures were 41.7 and 49.4 °C with and without TEG integration, respectively, corresponding

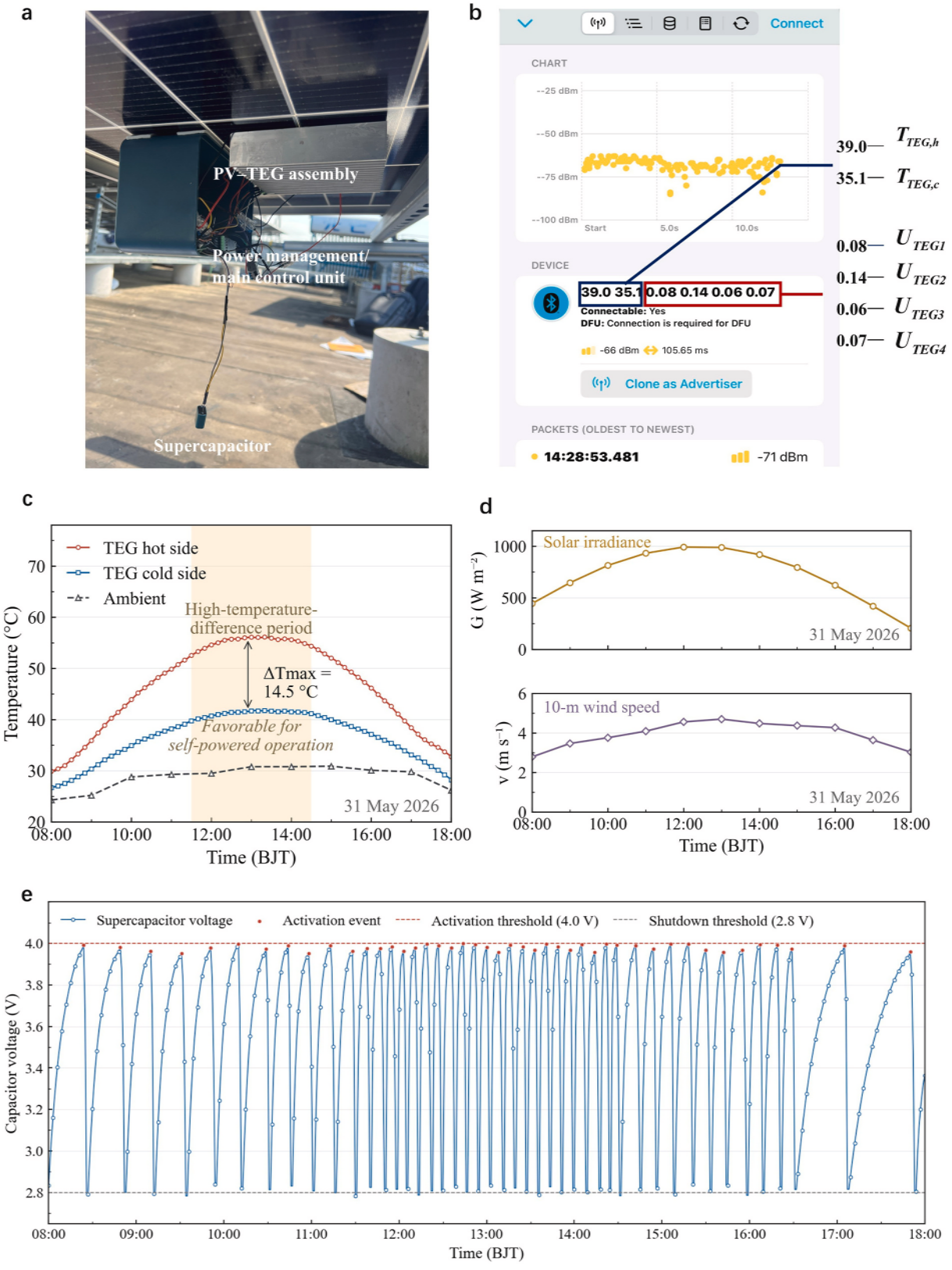


Fig. 7. Outdoor operation of the self-powered PV–TEG monitoring system: (a) field-deployed prototype; (b) wireless receiver interface; (c) TEG hot- and cold-side temperatures with ambient temperature; (d) solar irradiance and wind speed; and (e) supercapacitor-voltage cycles and activation events.

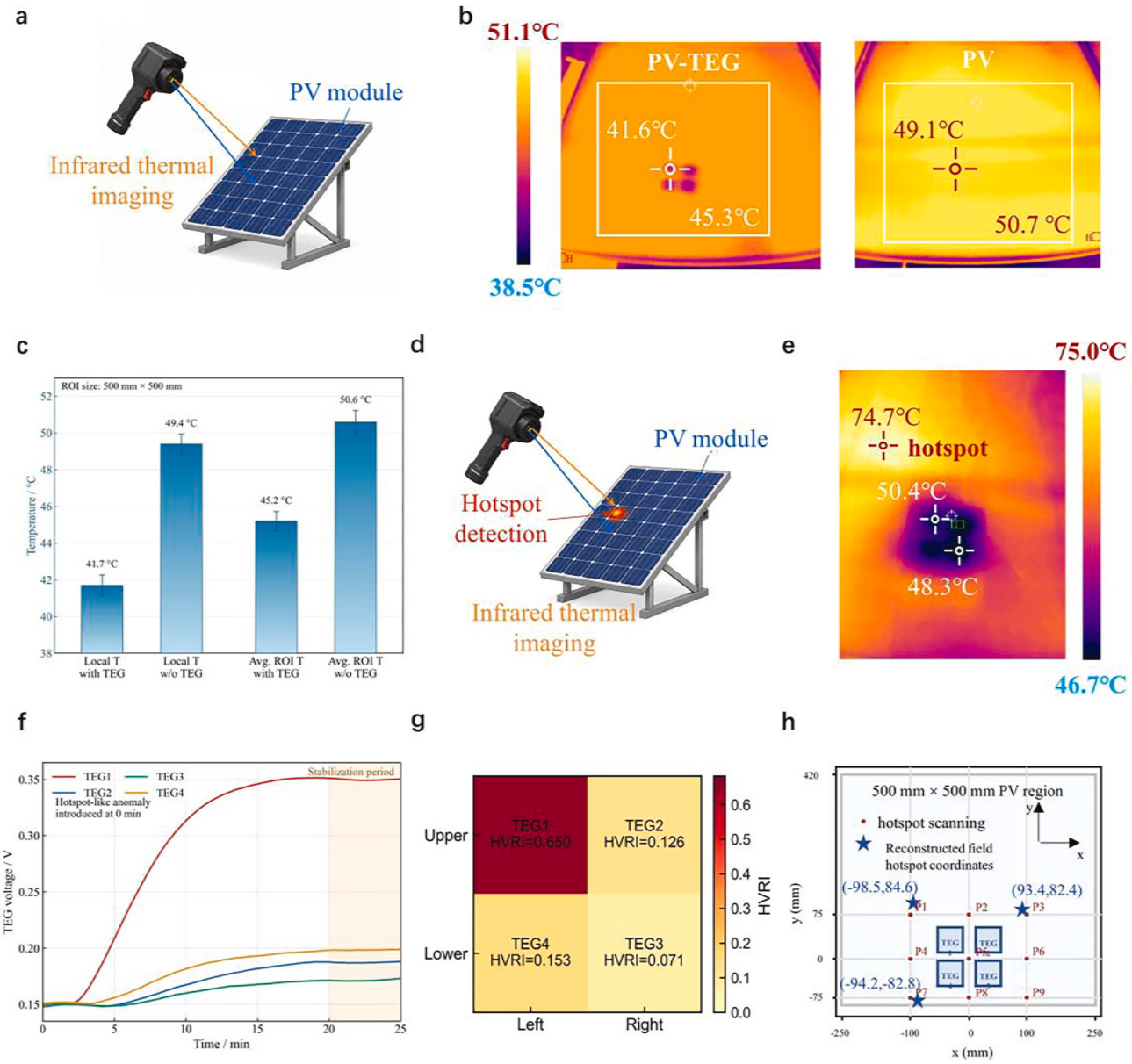


Fig. 8. Outdoor validation of local thermal management and voltage-based hotspot localization: (a) infrared thermography setup for thermal comparison; (b) thermal images of the PV–TEG and reference PV regions; (c) comparison of the measured point and regional-average temperatures between the reference PV and PV–TEG regions; (d) controlled hotspot-like anomaly test; (e) infrared image of the tape-induced thermal anomaly; (f) transient voltage responses of the four TEGs; (g) stable-state HVRI matrix; and (h) comparison between the prescribed and mean reconstructed coordinates for P1, P3, and P7.

to a temperature reduction of 7.7 °C. For the 500 mm × 500 mm region of interest (ROI), the corresponding mean temperatures were 45.2 and 50.6 °C, yielding an average reduction of 5.4 °C. Detailed trial-level results and repeatability statistics are provided in Section S5 of the Supplementary Information.

P1 is presented as the detailed representative localization case in Fig. 8(d–g). The infrared image shows a localized temperature rise to approximately 74.7 °C, while the four-channel response is dominated by TEG1, followed by TEG4. The corresponding mean HVRI values were approximately 0.650, 0.126, 0.071, and 0.153 for TEG1–TEG4, with $\xi = -0.606$ and $\zeta = 0.552$. The mean reconstructed coordinate of P1 was (−98.5, 84.6) mm; the mean trial-level localization error was approximately 9.9 mm. Fig. 8(h) further summarizes the prescribed and mean reconstructed coordinates for all three outdoor validation positions. P3 and P7 were reconstructed at (93.4, 82.4) and (−94.2, −82.8) mm, respectively, and all three reconstructed positions retained the correct spatial directions relative to the TEG array.

Two additional outdoor positions, P3 and P7, were further examined to assess the spatial representativeness of the localization method. TEG2 and TEG4 exhibited the dominant responses for the upper-right P3 and lower-left P7 anomalies, respectively. Across the three tested positions, the overall localization error was approximately 9.93 mm. Detailed multi-position infrared results, trial-level localization results, and repeatability statistics are provided in Section S5 of the Supplementary Information.

The black-tape-induced anomaly should be distinguished from an electrically induced PV hotspot. The tape produces local heating primarily by increasing solar absorption, whereas practical PV hotspots may involve electrical mismatch, partial shading, reverse-bias operation, interconnection defects, or material degradation accompanied by current redistribution and Joule heating. Consequently, their heat-generation profiles, spatial extents, temporal evolution, and peak

temperatures may differ. The present experiments therefore validate localization under controlled hotspot-like thermal disturbances rather than establishing a universal accuracy for electrically induced PV hotspots.

5. Conclusion

This study proposed a self-powered PV–TEG system integrating hotspot sensing, local thermal management, thermoelectric energy harvesting, and wireless transmission. Using the spatially differentiated outputs of a rear-side 2 × 2 TEG array, the system extends TEG functionality from waste-heat recovery to distributed thermal-field sensing. Numerical and outdoor tests confirmed the feasibility of the proposed framework. The main conclusions are as follows:

1. Multiphysics simulations clarified the coupling among hotspot position, thermoelectric voltage response, and local cooling. Distinct hotspot locations generated differentiated four-channel voltage patterns, enabling quantitative mapping from normalized voltage responses to two-dimensional coordinates. The simulated local temperature reduction ranged from 8.15 to 12.40 K.
2. The outdoor test in Taizhou, China, verified self-powered wireless operation. From 08:00 to 18:00, the TEGs repeatedly charged the supercapacitor between 2.8 and 4.0 V, supporting temperature and voltage acquisition and approximately 45 wireless transmissions to a mobile terminal.
3. Infrared measurements confirmed the local thermal-management effect. Relative to the reference PV region, the TEG-covered point and local-area average temperatures decreased by 7.7 and 5.4 °C, respectively, demonstrating the capability of the PV–TEG structure to mitigate local heat accumulation.
4. For the controlled black-tape-induced hotspot-like thermal anomaly, the normalized voltage-centroid method reconstructed the anomaly position with an error of 9.93 mm without directional misclassification. This result demonstrates the feasibility of the distributed TEG voltage matrix for local thermal-anomaly localization, while quantitative transfer of the mapping to electrically induced PV hotspots requires further validation.

Declaration of competing interest

The authors declare that they have no known competing financial interests or personal relationships that could have appeared to influence the work reported in this paper.

Acknowledgement

The work described in this paper is supported by the National Key Research and Development Program of China (grant number 2024YFB3715000) and the Smart Grid-National Science and Technology Major Project (2030) [grant number 2026ZD0809700].

Appendix A. Supplementary data

Supplementary data to this article can be found online at https://doi.org/10.1016/j.applthermaleng.2026.133776.

Data availability

Data will be made available on request.

References

[1] M. Victoria, N. Haegel, I.M. Peters, R. Sinton, A. Jäger-Waldau, C. del Cañizo, et al., Solar photovoltaics is ready to power a sustainable future, Joule 5 (2021) 1041–1056.
[2] K. Alberi, I.M. Peters, P. Verlinden, S. Philipps, A. Koike, T. Barnes, et al., Historical and future learning for the new era of multi-terawatt photovoltaics, Nat. Energy 11 (2026) 38–46.
[3] K.H. Chen, J. Zuo, R.D. Chang, Compendium of degradation rates of global photovoltaic (PV) technology: insights from technology, climate and geography, Sol. Energy Mater. Sol. Cells 293 (2025) 113839.
[4] Z.S. Jundi, A.H.A. Al-Waeli, N.T. Switzner, A systematic review of low-cost photovoltaic monitoring systems: technologies, challenges, and opportunities, Renew. Sust. Energ. Rev. 226 (2026) 116417.
[5] J.A. Tsanakas, L. Ha, C. Buerhop, Faults and infrared thermographic diagnosis in operating c-Si photovoltaic modules: a review of research and future challenges, Renew. Sust. Energ. Rev. 62 (2016) 695–709.
[6] F.G. Cabo, I. Marinic-Kragic, T. Garma, S. Nizetic, Development of thermo-electrical model of photovoltaic panel under hot-spot conditions with experimental validation, Energy 230 (2021) 120785.
[7] Y. Song, L. Huang, Y. Wang, Y.H. Du, Z.H. Song, Q.C. Dong, et al., Energy performance and fire risk of solar PV panels under partial shading: an experimental study, Renew. Energy 246 (2025) 122910.
[8] C.E. Clement, J.P. Singh, Y.S. Khoo, A. Halm, D. Tune, E. Birgersson, Design of shading- and hotspot-resistant shingled modules, Prog. Photovolt. 30 (2022) 464–480.
[9] M. Dhimish, Assessing MPPT techniques on hot-spotted and partially shaded photovoltaic modules: comprehensive review based on experimental data, IEEE Trans. Electron Devices 66 (2019) 1132–1144.
[10] E. Özkalay, F. Valoti, M. Caccivio, A. Virtuani, G. Friesen, C. Ballif, The effect of partial shading on the reliability of photovoltaic modules in the built-environment, EPJ Photovoltaics. 15 (2024) 7.
[11] C. Dunderdale, W. Brettenny, C. Clohessy, E.E. van Dyk, Photovoltaic defect classification through thermal infrared imaging using a machine learning approach, Prog. Photovolt. 28 (2020) 177–188.
[12] J. Teubner, C. Buerhop, T. Pickel, J. Hauch, C. Camus, C.J. Brabec, Quantitative assessment of the power loss of silicon PV modules by IR thermography and its dependence on data-filtering criteria, Prog. Photovolt. 27 (2019) 856–868.
[13] A.H. Herraiz, A.P. Marugán, F.P.G. Márquez, Photovoltaic plant condition monitoring using thermal images analysis by convolutional neural network-based structure, Renew. Energy 153 (2020) 334–348.
[14] N. Kellil, A. Aissat, A. Mellit, Fault diagnosis of photovoltaic modules using deep neural networks and infrared images under Algerian climatic conditions, Energy 263 (2023) 125902.
[15] R.L. Tang, Z.Y. Ren, S.W. Ning, Y. Zhang, Fault classification of photovoltaic module infrared images based on transfer learning and interpretable convolutional neural network, Sol. Energy 276 (2024) 112703.
[16] I.S. Ramírez, F.P.G. Márquez, J.P. Chaparro, Convolutional neural networks and internet of things for fault detection by aerial monitoring of photovoltaic solar plants, Measurement 234 (2024) 114861.
[17] A. Mellit, An embedded solution for fault detection and diagnosis of photovoltaic modules using thermographic images and deep convolutional neural networks, Eng. Appl. Artif. Intell. 116 (2022) 105459.
[18] B.J. Li, C. Delpha, A. Migan-Dubois, D. Diallo, Fault diagnosis of photovoltaic panels using full I-V characteristics and machine learning techniques, Energy Convers. Manag. 248 (2021) 114785.
[19] K. Ding, X. Chen, M. Jiang, H. Yang, X.H. Chen, J.W. Zhang, et al., Feature extraction and fault diagnosis of photovoltaic array based on conversion, Appl. Energy 353 (2024) 122135.
[20] H.G. Teo, P.S. Lee, M.N.A. Hawlader, An active cooling system for photovoltaic modules, Appl. Energy 90 (2012) 309–315.
[21] M.M. Islam, A.K. Pandey, M. Hasanuzzaman, N.A. Rahim, Recent progresses and achievements in photovoltaic-phase change material technology: a review with special treatment on photovoltaic thermal-phase change material systems, Energy Convers. Manag. 126 (2016) 177–204.
[22] Y.T. Liu, D.W. Yang, J. Lyu, J.H. Li, Z.M. Li, M.Y. Liu, et al., Integrated micro thermoelectric devices with self-power supply and temperature monitoring: design and application in power grid early warning, Appl. Therm. Eng. 247 (2024) 122922.
[23] S.M. Al Shurafa, F.B. Ismail, H.A. Kazem, T.A.H. Almajali, T.E. Sann, Experimental study of photovoltaic-thermoelectric systems using thermal interface materials and natural cooling, Appl. Therm. Eng. 258 (2025) 124855.
[24] E.S. Yin, Q. Li, Y.M. Xuan, Optimal design method for concentrating photovoltaic-thermoelectric hybrid system, Appl. Energy 226 (2018) 320–329.
[25] W.B. Gu, T. Ma, A.T. Song, M. Li, L. Shen, Mathematical modelling and performance evaluation of a hybrid photovoltaic-thermoelectric system, Energy Convers. Manag. 198 (2019) 111800.
[26] B. Lorenzi, P. Mariani, A. Reale, A. Di Carlo, G. Chen, D. Narducci, Practical development of efficient thermoelectric-photovoltaic hybrid systems based on wide-gap solar cells, Appl. Energy 300 (2021) 117343.
[27] N. Wang, L.L. Ni, A. Wang, H.S. Shan, H.Z. Jia, L. Zuo, High-efficiency photovoltaic-thermoelectric hybrid energy harvesting system based on functionally multiplexed intelligent thermal management, Energy Convers. Manag. 272 (2022) 116377.
[28] H. Ding, R. Guo, H. Xing, Y. Chen, J. He, J. Luo, et al., Spatial–temporal hotspot management of photovoltaic modules based on Fiber Bragg grating sensor arrays, Sensors 25 (2025) 4879.
[29] B. Guzowski, M. Lakomski, D. Bobinski, Hotspot detection in photovoltaic modules with Fiber Bragg grating and Brillouin distributed temperature sensors, Energies 18 (2025) 6117.

[30] M.U. Ali, A. Zafar, W. Ahmed, M. Aslam, S.H. Kim, Enhancing photovoltaic reliability: a global and local feature selection approach with improved Harris hawks optimization for efficient hotspot detection using infrared imaging, Int. J. Energy Res. 2024 (2024) 5586605.
[31] Y. Lee, N. Park, Self-powered wireless sensor system utilizing a thermoelectric generator for photovoltaic module monitoring application, Sol. Energy 283 (2024) 113026.
[32] W.H. Chen, C.Y. Liao, C.I. Hung, W.L. Huang, Experimental study on thermoelectric modules for power generation at various operating conditions, Energy 45 (2012) 874–881.
[33] M.H. Ge, Z.H. Li, Y.T. Zhao, Z.W. Xuan, Y.Z. Li, Y.L. Zhao, Experimental study of thermoelectric generator with different numbers of modules for waste heat recovery, Appl. Energy 322 (2022) 119523.
[34] E. Yin, Q. Li, Y.M. Xuan, Thermal resistance analysis and optimization of photovoltaic-thermoelectric hybrid system, Energy Convers. Manag. 143 (2017) 188–202.
[35] H.R.F. Kohan, M. Eslami, K. Jafarpur, Thermal influence of thermoelectric modules on performance of hybrid PV-TEG systems: effects of TEG type, arrangement and working condition, Int. Commun. Heat Mass Transfer 147 (2023) 106969.
[36] Y.Z. Gao, Z.F. Dai, D.X. Wu, C.L. Wang, B. Chen, X.S. Zhang, Transient performance assessment of a hybrid PV-TEG system integrated with PCM under non-uniform radiation conditions: a numerical investigation, Renew. Energy 198 (2022) 352–366.
[37] F.J. Montero, R. Lamba, A. Ortega, W. Jahn, W.H. Chen, A.M. Guzmán, A bidirectional solar thermoelectric generator combining heat storage for daytime and nighttime power generation, Appl. Therm. Eng. 224 (2023) 119997.
[38] M.M. Abdel-Aziz, A.A. ElBahloul, Enhanced photovoltaic cooling using sorption material with comparative evaluation of different fin geometries: a computational approach, Int. Commun. Heat Mass Transfer 169 (2025) 109928.
[39] C.Y. Li, Z.Y. Pei, Y.Z. Lin, W.J. Xie, N. Ukrainczyk, E.A.B. Koenders, et al., Thermoelectric brick with solid-solid phase change materials for building-integrated energy harvesting: design, simulation, and global evaluation, Appl. Therm. Eng. 282 (2026) 128844.
[40] R. Goswami, R. Das, Waste heat recovery from a biomass heat engine for thermoelectric power generation using two-phase thermosyphons, Renew. Energy 148 (2020) 1280–1291.
[41] C. Idogho, E.O. Abah, T. Imbur, K. Omenka, I.P. Idoko, Numerical simulation and synthesized material ranking for high-temperature thermoelectric power generation, Energy Technol. 14 (2026) e202502104.
[42] J. Xue, F.Y. Li, A.R. Fan, W.G. Ma, X. Zhang, Optimizing interfacial thermal resistance in GaN/AlN heterostructures: the impact of AlN layer thickness, Int. J. Heat Mass Transf. 239 (2025) 126629.
[43] S. Shittu, G.Q. Li, X.D. Zhao, X.L. Ma, Y.G. Akhlaghi, Y. Fan, Comprehensive study and optimization of concentrated photovoltaic-thermoelectric considering all contact resistances, Energy Convers. Manag. 205 (2020) 112422.
[44] B.W. Xiong, J.Y. Zhang, T.J. Liao, Y. Zhao, Z.H. He, Z.M. Yang, Theoretical and experimental analyses and optimizations of direct coupling photovoltaic-thermoelectric systems, Energy 307 (2024) 132688.
[45] A. Azirul, A. Ibrahim, N.S. Nazri, H. Jarimi, M. Zainuri, U. Syafiq, PVTE system performance improvement via numerical optimization of heat sink design and fluid working conditions, Sci. Rep. 15 (2025) 13586.
[46] A. Ashfaq, U. Khalique, A. Nadeem, A.A. Rizvi, Comprehensive analysis of temperature distribution in OPGW cable considering ramifications of short circuit current, Sci. Rep. 15 (2025) 21949.
[47] G. Huang, A.R. Yengannagari, K. Matsumori, P. Patel, A. Datla, K. Trindade, et al., Radiative cooling and indoor light management enabled by a transparent and self-cleaning polymer-based metamaterial, Nat. Commun. 15 (2024) 3798.
[48] A. Wang, Y.M. Xuan, Multiscale prediction of localized hot-spot phenomena in solar cells, Renew. Energy 146 (2020) 1292–1300.
[49] C. Zhang, H. Shen, J. Chen, H. Li, Relationship between module performance and the shading area for modules with different circuit connection mode, Semicond. Sci. Technol. 37 (2022) 025015.
[50] Z. Liu, Y. Gong, Z. Wang, Y. Li, D. Liu, Revealing the intrinsic mechanisms of hot and cold spots within a locally shaded photovoltaic module based on micro-electrical characteristics, Energies 17 (2024) 4462.
[51] N. Kumari, S.K. Singh, S. Kumar, V.K. Jadoun, Performance analysis of partially shaded high-efficiency mono PERC/mono crystalline PV module under indoor and environmental conditions, Sci. Rep. 14 (2024) 21587.